Journal of Energy Chemistry 65 (2022) 574–582

Contents lists available at ScienceDirect

Journal of Energy Chemistry

journal homepage: www.elsevier.com/locate/jechem

http://www.journals.elsevier.com/journal-of-energy-chemistry/

Interface engineering of porous Fe_2P-$WO_{2.92}$ catalyst with oxygen vacancies for highly active and stable large-current oxygen evolution and overall water splitting

Qimin Peng [a], Qiuting He [a], Yan Hu [a], Tayirjan Taylor Isimjan [b,*], Ruobing Hou [a], Xiulin Yang [a,*]

[a] Guangxi Key Laboratory of Low Carbon Energy Materials, School of Chemistry and Pharmaceutical Sciences, Guangxi Normal University, Guilin 541004, Guangxi, China
[b] Saudi Arabia Basic Industries Corporation (SABIC) at King Abdullah University of Science and Technology (KAUST), Thuwal 23955-6900, Saudi Arabia

ARTICLE INFO

Article history:
Received 26 March 2021
Revised 17 June 2021
Accepted 26 June 2021
Available online 15 July 2021

Keywords:
Fe_2P-$WO_{2.92}$
Interface engineering
Oxygen vacancy
Oxygen evolution
Overall water splitting

ABSTRACT

Constructing a low cost, and high-efficiency oxygen evolution reaction (OER) electrocatalyst is of great significance for improving the performance of alkaline electrolyzer, which is still suffering from high-energy consumption. Herein, we created a porous iron phosphide and tungsten oxide self-supporting electrocatalyst with oxygen-containing vacancies on foam nickel (Fe_2P-$WO_{2.92}$/NF) through a facile *in-situ* growth, etching and phosphating strategies. The sequence-controllable strategy will not only generate oxygen vacancies and improve the charge transfer between Fe_2P and $WO_{2.92}$ components, but also improve the catalyst porosity and expose more active sites. Electrochemical studies illustrate that the Fe_2P-$WO_{2.92}$/NF catalyst presents good OER activity with a low overpotential of 267 mV at 100 mA cm^{-2}, a small Tafel slope of 46.3 mV dec^{-1}, high electrical conductivity, and reliable stability at high current density (100 mA cm^{-2} for over 60 h in 1.0 M KOH solution). Most significantly, the operating cell voltage of Fe_2P-$WO_{2.92}$/NF || Pt/C is as low as 1.90 V at 400 mA cm^{-2} in alkaline condition, which is one of the lowest reported in the literature. The electrocatalytic mechanism shows that the oxygen vacancies and the synergy between Fe_2P and $WO_{2.92}$ can adjust the electronic structure and provide more reaction sites, thereby synergistically increasing OER activity. This work provides a feasible strategy to fabricate high-efficiency and stable non-noble metal OER electrocatalysts on the engineering interface.

Introduction

With the rapid development of the global economy, the continuous consumption of fossil fuels has caused a series of problems to the environment and public health, which is of utmost urgency to explore clean and renewable energy sources [1]. Hydrogen, as a clean energy source with high energy density and zero-emission, is an ideal alternative. Hydrogen production through electrochemical water splitting is a sustainable, efficient, and promising technology for converting and reserving green energy [2,3], which consists of two half-reactions, including the oxygen evolution reaction (OER) at the anode and the hydrogen evolution reaction (HER) at the cathode [4]. However, both HER/OER catalysts require high overpotentials making the water splitting one of the most energy-demanding processes. Especially, the OER catalyst demands much higher overpotential than that of HER, owing to its sluggish four-electron transfer kinetics ($2H_2O = 4H^+ + O_2 + 4e^-$) [5]. Therefore reducing the OER overpotential is the key step to improve the overall water splitting efficiency for practical applications. So far, the precious metal Ru and Ir oxides and their alloys-based catalysts are the most efficient OER electrocatalysts. Nevertheless, their industrial application is limited by their high cost, low durability, and scarcity [6,7]. Consequently, developing high-efficiency, low-cost and earth-abundant non-precious metal electrocatalysts for OER has important practical significance [8]. In recent years, in order to reduce cost and energy consumption, various OER catalysts based on non-noble metals contain transition metal oxides [9,10], hydroxides [11], (oxy)hydroxides [12], nitrides [13], phosphides [14,15], carbides [16], chalcogenides [17], borides [18] and carbon-based materials [8], have all been widely researched. Among them, transition metal phosphide-based (TMPs) catalysts have received extensive attention thanks to their good catalytic activity, high conductivity, robust stability, economic viability and exclusive redox properties [19,20].

* Corresponding authors.
E-mail addresses: isimjant@sabic.com (T.T. Isimjan), xlyang@gxnu.edu.cn (X. Yang).

https://doi.org/10.1016/j.jechem.2021.06.037

Additionally, tungsten-based materials and their various dopants are usually regarded as promising oxygen-evolving electrocatalysts under alkaline conditions [21]. Besides, oxides and phosphides have been extensively used for electrocatalytic oxygen-evolving, since metal oxides can effectively promote the dissociation of water, while phosphides have strong corrosion resistance, large electron density, and high electrical conductivity [22]. It is worth noting that the OER intrinsic activity of Tungsten oxide can be boosted significantly by increasing the oxygen vacancies, which can be adjusted by changing its band gaps and surface morphology [23,24]. Most importantly, self-supported tungsten oxide is proven to be a reliable electro-catalyst, due to the abundant active sites and porosity that promotes gas diffusion and effective electron transfer in the electrochemical reaction process [25]. Moreover, the self-supported tungsten oxide has a robust structure and stable in an alkaline medium [26]. Based on the above consideration, we can safely assume that self-supported and transition metal phosphate doped tungsten oxides have the potential to be an efficient OER catalyst.

Here, we constructed a porous Fe_2P-$WO_{2.92}$/NF catalyst through a controllable method, including conventional hydrothermal *in-situ* growth, soaking and gas phase phosphating treatments. We have used a variety of techniques to characterize the hybrid catalyst in detail, and confirmed the composition, crystal structure, porosity, microscopic morphology and electronic structure of the catalyst. Electrochemical studies demonstrate that Fe_2P-$WO_{2.92}$/NF exhibits good OER properties with an impressively low overpotential of 215 mV to yield 10 mA cm^{-2} and a small Tafel slope of 46.3 mV dec^{-1} comparable to commercial RuO_2 catalyst. Moreover, the Fe_2P-$WO_{2.92}$/NF catalyst also performs robust overall water splitting activity both at low and high current densities. For instance, the Fe_2P-$WO_{2.92}$/$NF^{(+)}$ || $Pt/C^{(-)}$ two-electrode system can reach 10 mA cm^{-2} at 1.49 V and 400 mA cm^{-2} at 1.90 V, even better than the state-of-the-art $RuO_2^{(+)}$ || $Pt/C^{(-)}$. In addition, the Fe_2P-$WO_{2.92}$/$NF^{(+)}$ || $Pt/C^{(-)}$ electrolyzer also shows a long-term stability at 400 mA cm^{-2} with almost no degradation under simulated industrialization conditions, indicating a significant potential for industrial application.

Experimental section

Materials and chemicals

Sodium tungstate dihydrate ($Na_2WO_4{\cdot}2H_2O$, 99.5%), potassium hydroxide (KOH, 90%), potassium ferricyanide ($K_3[Fe(CN)_6]$, 99.5%), ethanol (C_2H_5OH, 99.7%), sodium hypophosphite monohydrate ($NaH_2PO_2{\cdot}H_2O$, 99%), and hydrochloric acid (HCl, 37%) are analytical grade and were used without further purification. Nickel foam (NF, thickness: 1.6 mm) was obtained from commercial source. Nafion solution (5 wt%) and commercial Pt/C (20 wt% for platinum) were purchased from Alfa Aesar. Deionized water was used in the experiments.

Synthesis of WO_3/NF

A piece of NF (2 cm × 3 cm) was washed with 0.5 M HCl, deionized water and ethanol under ultrasonic vibration for 15 min respectively to ensure that the surface was clean. Briefly, 1 mmol $Na_2WO_4{\cdot}2H_2O$ were dissolved in 50 mL deionized water to form a homogeneous solution under magnetic stirring at room temperature, and then a 3 M HCl aqueous solution was added slowly to regulate the pH value of the above-prepared solution (pH = 2–3). After continuous stirring for 30 min, the resulting solution and NF were transferred into a Teflon-lined stainless steel autoclave (90 mL) and maintained at 180 °C for 6 h in an electric oven and cooled naturally to room temperature. The obtained product (Named as WO_3/NF) was washed several times with ethanol and deionized water, and then dried at 60 °C for 3 h.

Synthesis of Fe_2P-$WO_{2.92}$/NF composite

The target Fe_2P-$WO_{2.92}$/NF was fabricated via a facile two-step procedures, including $K_3[Fe(CN)_6]$ etching and phosphating subsequently. In the first step, a piece of WO_3/NF has soaked into a 0.1 M $K_3[Fe(CN)_6]$ aqueous solution at room temperature, after soaking for 4 h, the resulted Fe-W-species/NF was taken out and washed several times with ethanol and water, and then dried in an oven at 60 °C for 3 h. Note that Fe-species/NF is prepared by using NF instead of WO_3/NF, other steps being the same. After that, 1.0 g $NaH_2PO_2{\cdot}H_2O$ and the pre-prepared Fe-W-species/NF were put at the upstream side and center of the tube furnace, respectively. The sample was heated to 350 °C (5 °C min^{-1}) and annealed for 120 min under a high-purity N_2 atmosphere. After naturally cooling to room temperature, the obtained product was named as Fe_2P-$WO_{2.92}$/NF. As a control, the preparation of Fe_2P/NF and $WO_{2.92}$/NF is similar to that of Fe_2P-$WO_{2.92}$/NF, except that Fe-W-species/NF is replaced by precursors of Fe-species/NF and WO_3/NF for phosphating treatment.

Preparation of RuO_2 and 20 wt% Pt/C electrodes

The commercial $RuCl_3{\cdot}3H_2O$ was directly calcined at 400 °C for 3 h in the air to obtain RuO_2 powders. And then 2 mg RuO_2 or 20 wt% commercial Pt/C was dispersed into a mixture of 245 μL deionized water, 245 μL ethanol and 10 μL 5 wt% Nafion, respectively. The mixture was ultrasonically treated for at least 30 min to form a uniform catalyst ink, then dropped onto the surface of NF (1 cm × 1 cm) and dried naturally in the air.

Material characterizations

The crystal and phase structures of samples were measured by X-ray diffraction (XRD, Rigaku D/Max 2500 V/PC, Cu K_α radiation). The morphologies of the samples were characterized by scanning electron microscopy (SEM, FEI Quanta 200) and transmission electron microscopy (TEM, JEM-2100F). The elemental chemical-states of the samples were analyzed by X-ray photoelectron spectroscopy (XPS, JPS-9010TR, Japan, Mg K_α radiation). The specific BET surface area and pore size distribution of the samples were obtained on a Quanta chrome instrument (BET, 3H-2000PS4). The actual loadings of different metals in the samples were detected by inductively coupled plasma atomic emission spectrometry (ICP-AES, IRIS Intrepid II XSP).

Electrochemical measurements

The electrocatalytic performance of the synthesized catalysts were evaluated on an electrochemical workstation (Biologic VMP3) with a standard three-electrode system in 1.0 M KOH (pH ≈ 13.5) electrolyte. The as-prepared NF-based catalysts electrode (with a working area of 1 × 1 cm^2) were used as the working electrode, the counter electrode and the reference electrode were graphite plate and saturated calomel electrode (SCE), respectively. Cyclic voltammetry (CV) test can achieve a stable electrocatalytic performance of the catalyst at a scan rate of 10 mV s^{-1} in the range of 0–0.8 V (*vs.* SCE). The electrochemical double layer capacitance (C_{dl}) of the catalysts were obtained by CV tests in a non-faradaic region with scan rates from 10 to 60 mV s^{-1} in 1.0 M KOH, and the C_{dl} can be calculated by the following equation [27]: $C_{dl} = (j_a\text{-}j_c)/(2 \times \nu)$, where j_a and j_c corresponds to the current density of anode and cathode, respectively, and ν is scan rate. The linear

sweep voltammetry (LSV) were recorded at a low scan rate of 0.2 mV s^{-1} in the range of 1.0–1.8 V (*vs.* RHE). The overpotential (η) of OER can be calculated by the following equation: η (V) = E_{RHE} − 1.23 V. Electrochemical impedance spectroscopy (EIS) measurements were conducted at 0.5 V (*vs.* SCE) with the frequency range from 0.1 Hz to 200 kHz. The long-term stability test of the catalysts were achieved by chronopotentiometry and chronoamperometry measurements at different current densities of 10 and 100 mA cm^{-2}, respectively. All potentials (*vs.* SCE) were calibrated by the equation of $E_{RHE} = E_{SCE} + 0.242 + 0.059 \times pH$ (Fig. S1). The overall water splitting test was performed in 1.0 M KOH and 30 % KOH (78.2 mL) electrolyte, separately, and the two electrode system in the potential range of 0–2.5 V (*vs.* SCE) with a scan rate of 5 mV s^{-1}. All reported curves had been corrected by *i*R compensation.

Results and discussion

Catalyst preparation

A facile consecutive three-step synthesis (*in-situ* hydrothermal growth, soaking, and phosphating) of Fe_2P-$WO_{2.92}$/NF is illustrated in Scheme 1. Specifically, the dark navy blue WO_3 is initially grown *in-situ* on the nickel foam by conventional hydrothermal treatment of Na_2WO_4 acid solution. Afterwards, the WO_3/NF was immersed in the $K_3[Fe(CN)_6]$ aqueous solution to obtain a yellow Fe-W-species/NF component. Ligand exchange happens between $Fe(CN)_6^{3+}$ and WO_3 that dissolves the WO_3, while the $Fe(OH)_3$ is deposited on the WO_3 in the water. This is consistent with the results obtained by ICP-MS test that the content of W decreases continuously with the prolonging of etching time (Table S1). Finally, Fe-W-species/NF is transformed into black Fe_2P-$WO_{2.92}$/NF composite through gas phase phosphating treatment (Fig. S2). The PH_3 gas was generated through the decomposition of $NaH_2PO_2{\cdot}H_2O$ [28]. During the phosphating, the PH_3 not only becomes a source of phosphorus but also acts as a reducing agent. In this process, part of the high-valence W (VI) in the precursor is reduced to W (V), accompanied by the generation of oxygen vacancies, meanwhile, the iron species is phosphatized into Fe_2P. The loading of Fe_2P-$WO_{2.92}$ on NF is about 1.25 mg cm^{-2}, which is obtained by accurately weighing the mass before and after loading.

Crystallinity, microstructure and porosity analysis

X-ray diffraction (XRD) patterns were collected to explore the chemical composition and crystallinity of the as-prepared catalysts. Fig. 1(a) exhibits the seven distinct diffraction peaks at 14.0°, 22.7°, 28.2°, 36.6°, 50.0°, 55.3° and 58.3° are attributed to (100), (001), (200), (201), (220), (202) and (400) lattice planes of the hexagonal WO_3 phase (JCPDS: 33–1387), respectively. The WO_3 sample is scraped from the surface of NF because the diffraction peak of NF is too strong to observe the diffraction peak of WO_3 species. As shown in Fig. 1(b), after the WO_3 component is treated by $K_3[Fe(CN)_6]$ and subsequent phosphating treatment, the representative three diffraction peaks at 23.3°, 40.8° and 54.4° can be indexed to the (010), (-4112) and (325) lattice planes of monoclinic $WO_{2.92}$ (JCPDS: 30–1387) [29,30], as well the other diffraction peaks located at 47.3° and 54.6° are matched well with the (210) and (211) lattice planes of the hexagonal Fe_2P phase (JCPDS: 51–0943). The $WO_{2.92}$ structure was identified by XRD pattern as reported by other studies [29–31].As a comparison, when a single WO_3/NF and $K_3[Fe(CN)_6]$ soaked hydrothermal NF were phosphatized, they were converted into $WO_{2.92}$/NF and Fe_2P /NF (Fig. S3), respectively. However, the diffraction intensity of $WO_{2.92}$ phase in Fe_2P-$WO_{2.92}$/NF is significantly higher than that of $WO_{2.92}$/NF, indicating the increased crystallinity caused by the interaction between Fe and W species [32]. Moreover, the Fe-W-species/NF component corresponds to WO_3 (JCPDS: 33–1387) and $Fe(OH)_3$ (JCPDS: 38–0032) (Fig. S4).

The morphological and microstructure of the catalysts were analyzed by scanning electron microscopy (SEM) and transmission electron microscopy (TEM). Fig. S5(a) shows that the surface of cleaned NF is a smooth three-dimensional structure. The SEM image in Fig. 2(a) indicates that the WO_3 was successfully grew on the NF surface, displaying a nanowires structure. Yet, after the WO_3/NF precursor is treated by $K_3[Fe(CN)_6]$, there are a lot of particulate materials on the surface of the porous structure, and the structure became more dense (Fig. 2b). Furthermore, after the phosphatization, the Fe_2P-$WO_{2.92}$/NF surface becomes smoother (Fig. 2c). Fig. S5(b – d) shows that the low-magnification SEM images of WO_3, Fe-W-species/NF and Fe_2P-$WO_{2.92}$/NF, respectively, showing that they grow uniformly on NF. To investigate the effect of morphological changes, the different Brunauer-Emmett–Teller (BET) surface area was measured by N_2 adsorption–desorption isotherm, and the isotherms of the catalysts display the typical III-type hysteresis loop in Fig. 1(c and d). The porous structured Fe_2P-$WO_{2.92}$ illustrate a comparatively large BET surface area of 6.6 m^2 g^{-1}, which is larger than that of $WO_{2.92}$ (5.2 m^2 g^{-1}). Besides, we also calculated the adsorption average pore diameters of Fe_2P-$WO_{2.92}$ (11.1 nm) and $WO_{2.92}$ (6.5 nm) by BJH method, which were mainly caused by cracks and porous structures in the composite [27]. The Fe_2P-$WO_{2.92}$ composite exhibits a larger

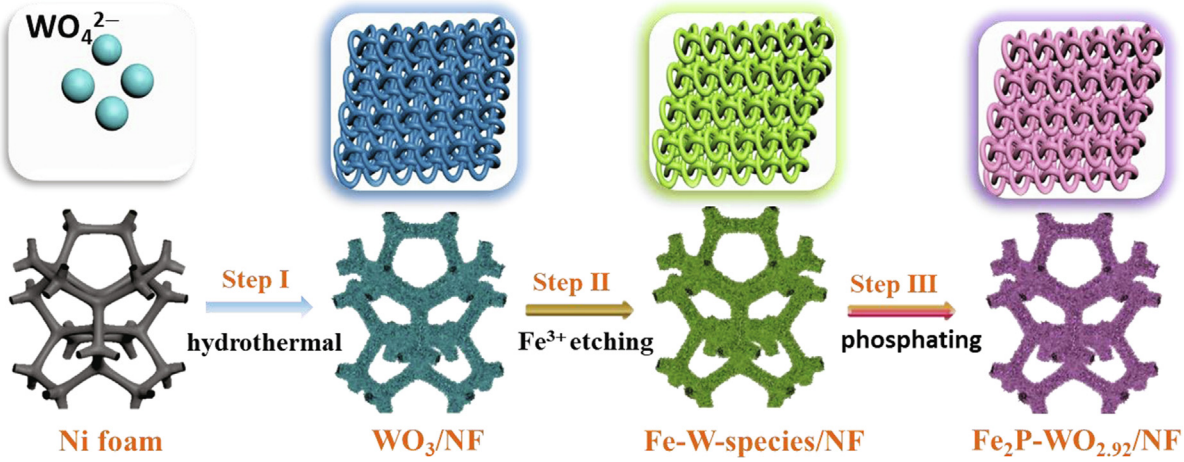

Scheme 1. Schematic illustration of the preparation process for Fe_2P-$WO_{2.92}$/NF catalyst.

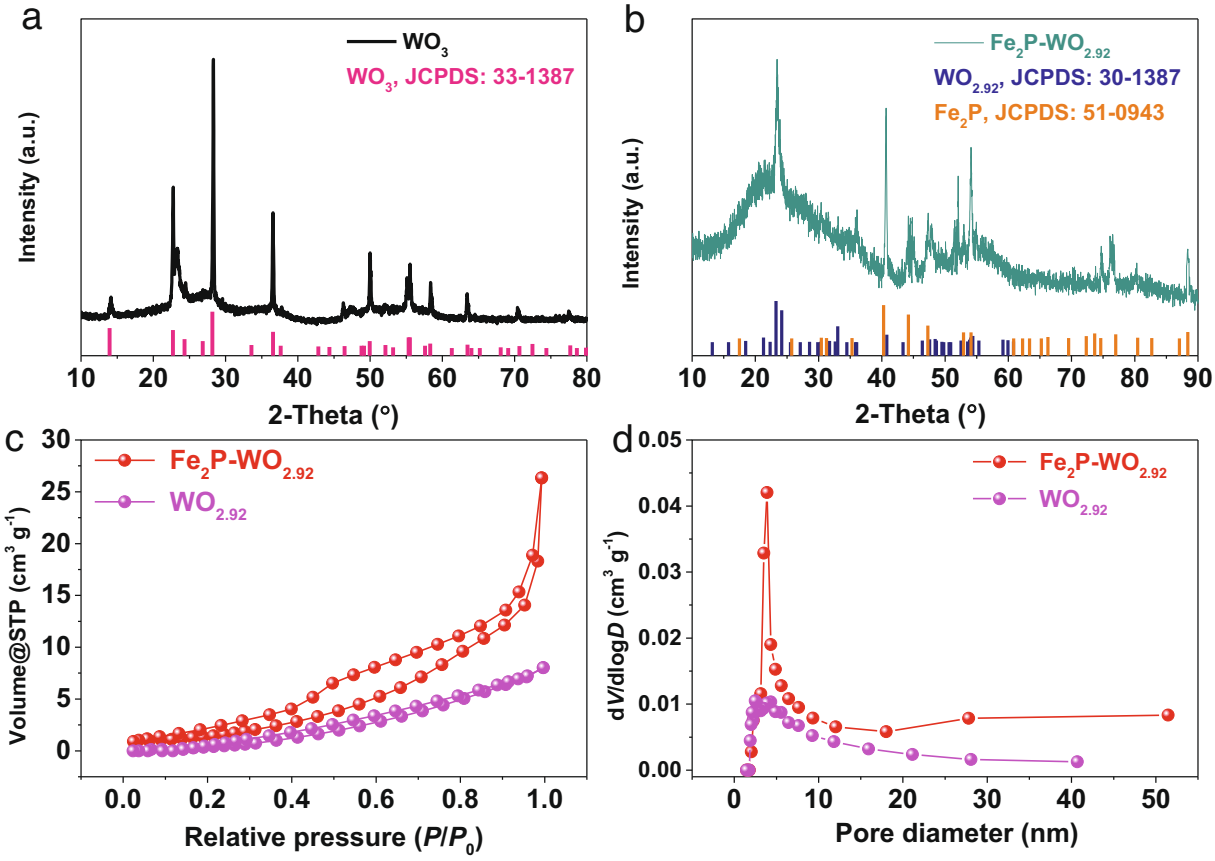

Fig. 1. XRD patterns of (a) WO_3 and (b) Fe_2P-$WO_{2.92}$. (c) N_2 adsorption/desorption isotherms, and (d) the pore size distribution curves by the BJH method of Fe_2P-$WO_{2.92}$ and $WO_{2.92}$.

BET surface area and average pore diameter could provide more active sites and faster mass transfer rate than $WO_{2.92}$ subsequently boosting OER catalytic activity. Besides, We also studied the morphologies of the contrast samples without $K_3[Fe(CN)_6]$ and W, named $WO_{2.92}$/NF and Fe_2P/NF. The $WO_{2.92}$/NF also has a porous structure, while the morphology of Fe_2P/NF looks like a bulk structure (Fig. S6). The Table S3 is the summary of OER performance of catalysts with different soaking time, we have found that the performance varies with the soaking time. In addition, the influence of hydrothermal and soaking time on the morphology of the catalysts are shown in Figs. S7 and S8. When the hydrothermal time is 4 h, the morphology of the precursor is a nanoflower formed by nanowires, and when the hydrothermal time is over 6 h, the morphology of the precursor is interlinked porous nanowires. The soaking time has no great influence on the morphology of the catalyst. After phosphating, the morphology is slightly changed, but the overall structure is porous, which is conducive to improving the catalytic activity of OER. The microstructure of Fe_2P-$WO_{2.92}$/NF were further observed by TEM and high-resolution TEM (HRTEM). Fig. 2(d) also shows that Fe_2P-$WO_{2.92}$/NF has a porous structure, which is consistent with the SEM results. The HRTEM image clearly reveals a series of lattice spacing such as 0.382 and 0.192 nm, corresponding to the (010) lattice plane of $WO_{2.92}$ and (210) lattice plane of Fe_2P (Fig. 2e). At the same time, the inset of Fig. 2e illustrates that the selected area electron diffraction (SAED) pattern also confirms the existence of (010) lattice plane for Fe_2P-$WO_{2.92}$/NF [33]. Due to the low crystallinity of Fe_2P in the catalyst, the presence of Fe_2P is not observed in the SAED pattern, indicating the polycrystalline characteristic of the catalyst. Energy dispersive X-ray (EDX) pattern (Fig. 2f) shows obvious signals of W, Fe, C, O and P in Fe_2P-$WO_{2.92}$/NF. The high-angle annular dark-field scanning TEM (HAADF-STEM) and EDX mapping images demonstrate that W, Fe, C, O, and P are uniformly distributed in the Fe_2P-$WO_{2.92}$/NF catalyst (Fig. 2g – l). The consequence of inductively coupled plasma mass spectrometry (ICP-MS) test reveals that the Fe_2P-$WO_{2.92}$/NF catalyst is composed of W (9.64 wt%) and Fe (43.09 wt%) (Table S1). Besides, from the EDX pattern, the rest are mainly O (56.73 wt%), C (8.80 wt%) and P (9.80 wt%) [31].

XPS analysis

X-ray photoelectron spectroscopy (XPS) was employed to further explore the composition, and surface chemical valence of the as-prepared catalysts. In the XPS spectrum, the oxidation state of the element is related to the peak position, and the peak area is directly proportional to the elemental content. As shown in Fig. S9a, the W, Fe, C, O and P elements can be clearly retrieved in the overall XPS spectra of Fe_2P-$WO_{2.92}$/NF, which is consistent with the results of EDX mapping. The high-resolution C 1 *s* spectrum of Fe_2P-$WO_{2.92}$/NF catalyst is deconvolved into C–C (284.8 eV), C-O (286.0 eV) and O = C-O (288.7 eV) and used as calibration standards for other elements (Fig. S9b) [34,35].

As shown in Fig. 3(a), the high-resolution Fe 2*p* spectra of Fe_2P-$WO_{2.92}$/NF and Fe_2P/NF are composed of Fe $2p_{1/2}$, Fe $2p_{3/2}$ regions and satellite peaks. Two of the diffraction peaks at 706.6 and 722.1 eV are typical Fe-P bonds, indicating the formation of Fe_2P components in the composite. In addition, the Fe $2p_{3/2}$ region can be further deconvolved into three peaks at 710.5, 713.5 and 717.0 eV, which are attributed to the existence of Fe^{2+} oxide, Fe^{3+} oxide and satellite peak respectively [36], while the oxidation peak

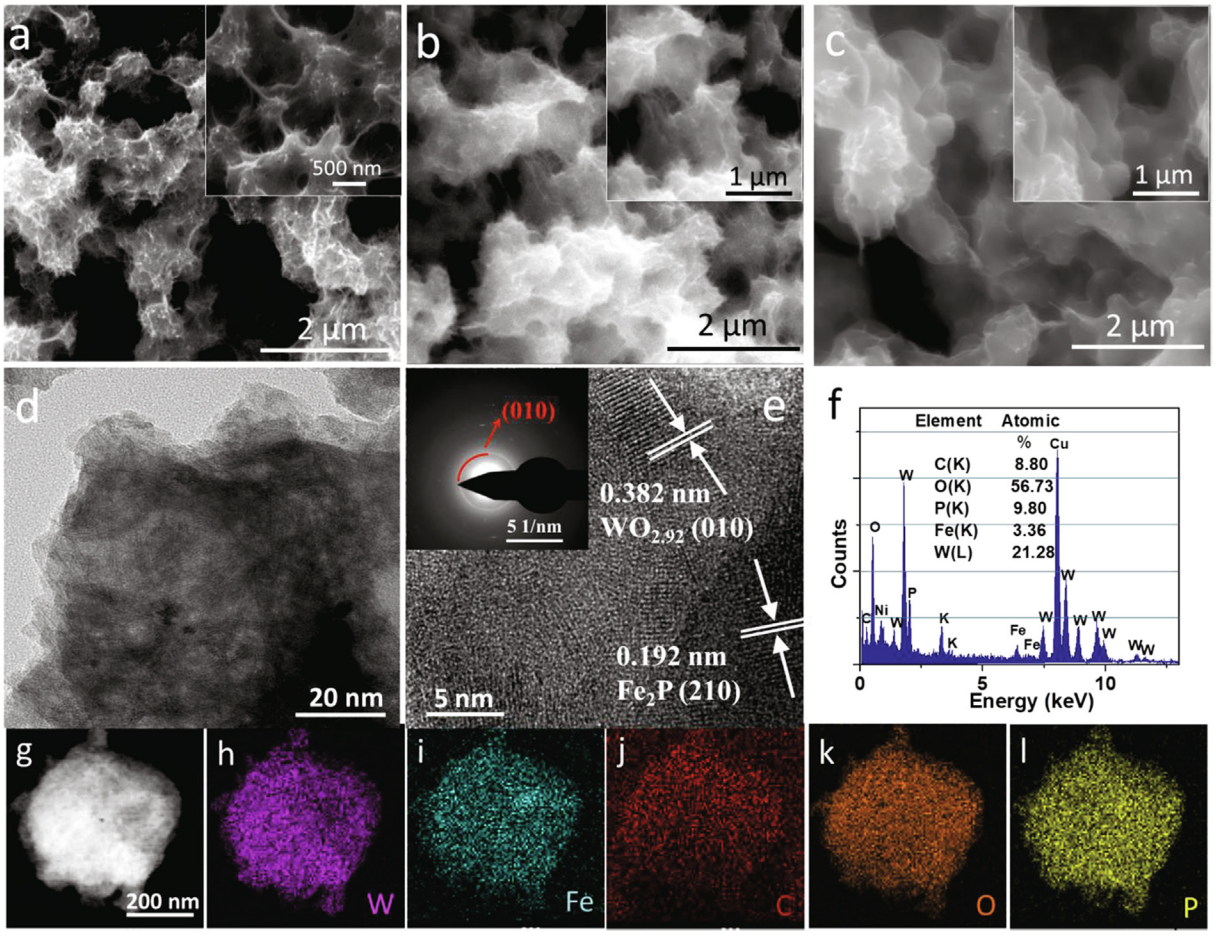

Fig. 2. Scanning electron microscopy (SEM) images of (a) WO_3, (b) Fe-W-species/NF, (c) Fe_2P-$WO_{2.92}$/NF. (d) Transmission electron microscopy (TEM) and (e) high- resolution TEM (HRTEM) images of the Fe_2P-$WO_{2.92}$/NF (inset: the SAED pattern). (f) EDX pattern of the Fe_2P-$WO_{2.92}$/NF. (g) HAADF-STEM image of the Fe_2P-$WO_{2.92}$/NF. (h l) the corresponding STEM-EDX elemental mappings of W, Fe, C, O and P.

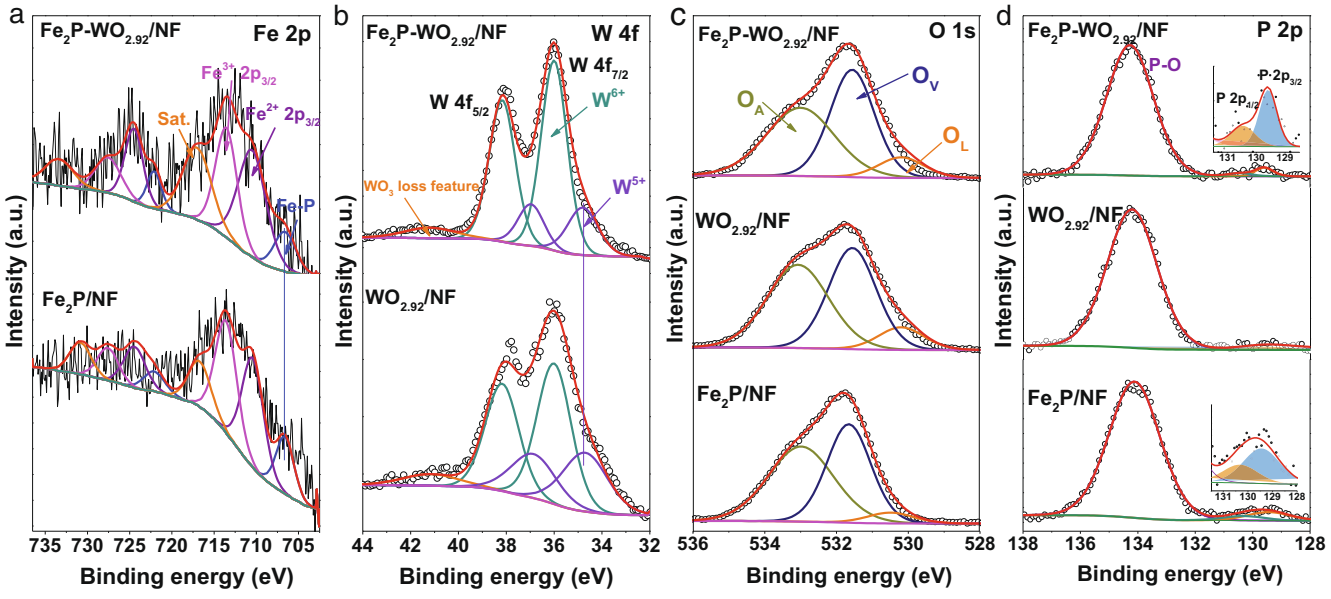

Fig. 3. High-resolution XPS spectra of (a) Fe 2*p*, (b) W 4*f*, (c) O 1 *s*, (d) P 2*p* for Fe_2P-$WO_{2.92}$/NF, $WO_{2.92}$/NF and Fe_2P/NF.

of Fe species may be caused by the oxidation of Fe_2P-$WO_{2.92}$/NF surface upon air and the Fe-O-W bond formed during the etching process [37]. The average valence state of W is 5.84 that composed of W^{5+} and W^{6+}. Generally, the binding energy of Fe 2*p* in Fe_2P is

higher than 707 eV [38], so the low binding energy of Fe 2*p* in Fe_2P-$WO_{2.92}$/NF composite indication charge transfer between $WO_{2.92}$ and Fe_2P component. Besides, the high-resolution spectra of W 4*f* (Fig. 3b) can be deconvoluted into five peaks, corresponding to the different oxidation states of W species such as W^{6+} (36.0 and 38.2 eV), W^{5+} (35.0 and 37.2 eV) and another small loss feature peak of WO_3 located at 41.2 eV [30]. The lower chemical valence of W^{5+} is formed during the phosphating of Fe_2P-$WO_{2.92}$/NF. Hence, the above results confirm the formation of tungsten oxide ($WO_{2.92}$) [31]. The W^{6+} species are partially reduced to W^{5+} by PH_3 during phosphatization. For comparison, Figs. S10 and S11 show that the high-resolution W 4*f* of WO_3/NF together with Fe 2*p* and W 4*f* of Fe-W-species/NF, the high-resolution spectra of W 4*f* can be deconvoluted into two peaks, corresponding to the oxidation states of W^{6+}. And the high-resolution Fe 2*p* spectra of Fe-W-species/NF are composed of Fe $2p_{1/2}$ and Fe $2p_{3/2}$ regions. The XRD (Fig. S4) and XPS (Fig. S11) indicated that W in the precursor WO_3 and Fe-W-species exist in the same form before and after Fe^{3+} etching meaning the etching step has no effect on oxygen vacancies. The oxygen vacancies formed during the phosphatization process through two steps, including metal ion reduction and phosphorous insertion (Figs. S4 and S11).

Besides, the high-resolution O 1 *s* spectra are used to examine the changes of oxygen species on the surface of different catalysts. The O 1 *s* XPS spectrum consists of three peaks with binding energies at approximately 530.2 eV, 531.5 eV and 533.0 eV, attributing to lattice oxygen (O_L), oxygen vacancies (O_V) and surface adsorbed oxygen species (O_A), respectively (Fig. 3c) [39]. Notably, from the O 1 *s* XPS spectrum, it can be concluded that there are certain oxygen vacancies in Fe_2P-$WO_{2.92}$/NF, indicating that the strong interaction between W and Fe can increase the concentration of O_V. The reason for the generation of O_V is that excessive PH_3 gas will take away part of the O atoms in WO_3 component to form compounds containing oxygen vacancies [37], As a result, the hexagonal WO_3 transform into monoclinic $WO_{2.92}$ in order to minimize the lattice stress. The $WO_{2.92}$ was formed through the lattice rearrangement because of the lattice stress resulted from oxygen vacancies. Moreover, a certain proportion of O_V in Fe_2P-$WO_{2.92}$/NF is consistent with the transfer of part of the electrons from $WO_{2.92}$ to the Fe_2P component. As shown in Fig. 3(d), the high-resolution P 2*p* spectrum mainly includes P $2p_{3/2}$ (129.6 eV) and P $2p_{1/2}$ (130.5 eV), as well as a typical broad peak of P-O bond at 134.3 eV [40]. These confirmed that the metal phosphide (Fe_2P) formed in the composite was partially oxidized on the surface. In short, XPS analysis suggests that the valence states of the catalyst elements have undergone subtle changes, demonstrating that the introduction of Fe_2P component is beneficial to enhance electronic interaction and redistribution, thereby synergistically improving OER activity.

Electrochemical performance analysis

The OER performance of different catalysts was evaluated by linear sweep voltammetry (LSV) in 1.0 M KOH solution with a typical three-electrode electrochemical system. We first optimized the effect of reaction conditions on the catalytic performance of Fe_2P-$WO_{2.92}$/NF. The study found that the best catalytic performance was obtained by hydrothermal time of 6 h (Figs. S12 and S13 and Table S2) and soaking time of 4 h (Table S3). As shown in Fig. 4 (a), the LSV polarization curves clearly demonstrated that the Fe_2P-$WO_{2.92}$/NF catalyst requires only 215 mV of overpotential at current density of 10 mA cm^{-2}, comparable to that of RuO_2 (213 mV), which is significantly lower than these of $WO_{2.92}$/NF (250 mV), Fe_2P/NF (235 mV) and NF (306 mV) (Table 1), indicating that the synergy between $WO_{2.92}$ and Fe_2P components is the key to improving OER activity. In particular, the overpotentials required for Fe_2P-$WO_{2.92}$/NF catalyst at higher current densities of 50 and 100 mA cm^{-2} are 249 and 267 mV respectively, and the advantages are more prominent compared with all other catalysts (Fig. 4b). To further evaluate the intrinsic catalytic activity, the corresponding Tafel slope calculated from LSV polarization curve was used to investigate the OER kinetics. As shown in Fig. 4(c), Fe_2P-$WO_{2.92}$/NF catalyst manifests a comparatively small Tafel plot of 46.3 mV dec^{-1}, which is much lower than those of $WO_{2.92}$/NF (93.8 mV dec^{-1}), Fe_2P/NF (62.7 mV dec^{-1}), RuO_2 (85.5 mV dec^{-1}) and NF (100.0 mV dec^{-1}), suggesting a fast OER kinetic reaction and high charge transfer coefficient of the Fe_2P-$WO_{2.92}$/NF [41,42]. Notably, this work is better than most of the previous reports in terms of both electrocatalytic OER overpotential and Tafel slope (Fig. 4d, Table S4), indicating that it has a significant contribution to the related field.

The electrochemically active surface area (ECSA), which is proportional to the double-layer capacitance (C_{dl}), is a critical parameter for studying the interfacial dynamics of electrode. The C_{dl} values of different catalysts are obtained from the CV curves using various scan rates in non-Faradaic potential regions (Figs. S15 – S18). As shown in Fig. 4(e), the C_{dl} of Fe_2P-$WO_{2.92}$/NF catalyst is 24.8 mF cm^{-2}, which is much higher than that of all control catalysts (Table 1). Meanwhile, the ECSA values are calculated according to the equation (1):

$$\mathrm{ECSA} = C_{dl}/C_S \quad (1)$$

where the C_S is 40 μF cm^{-2} [43,44]. The results revealed that the ECSA value of Fe_2P-$WO_{2.92}$/NF is 620 cm^2 (Fig. 5a), which is 2.3-, 2.3-, 1.6- and 3.8-fold higher than those of $WO_{2.92}$/NF, Fe_2P/NF, RuO_2 and NF, respectively. This largest ECSA means the most active sites, which is the intrinsic reason for the excellent OER performance of the catalyst.

In addition, we also compared Fe_2P-$WO_{2.92}$/NF and $WO_{2.92}$/NF with Fe_2P-WO_3/NF and WO_3/NF in terms of their performance and ECSA. Fig. S14 shows that Fe_2P-WO_3/NF and WO_3/NF require overpotentials of 244 mV and 263 mV at current density of 10 mA cm^{-2}, respectively. Moreover, the ECSA values of Fe_2P-WO_3/NF and WO_3/NF are 258 cm^2 and 163 cm^2, respectively, which is significantly lower than Fe_2P-$WO_{2.92}$/NF. These results further illustrate that the presence of oxygen vacancies can greatly increase OER activity and ECSA.

Moreover, the electrochemical impedance spectroscopy (EIS) was used to explore the electrode kinetics. In general, the charge transfer resistance (R_{ct}) of the catalyst refers to the semicircle diameter of the Nyquist plots, and the solution resistance (R_s) refers to the intersection of the semicircle and the x-axis. As shown in Figs. S19 and S20, the Fe_2P-$WO_{2.92}$/NF has the lowest R_{ct} (0.32 Ω) among the all catalysts, demonstrating high charge transfer efficiency and good conductivity.

Stability testing is an important criterion for evaluating the practical application of catalysts. The chronopotentiometry curve was used to explore the long-term stability of the Fe_2P-$WO_{2.92}$/NF catalyst in a three-electrode system. We observed that the potential of the Fe_2P-$WO_{2.92}$/NF catalyst only increased by about 8.4% after 100 h of continuous operation at 10 mA cm^{-2} (Fig. 4f), reflecting the robust stability and good activity retention under continuous operation. Besides, when the catalyst was operated at a high current density of 100 mA cm^{-2} for 60 h, a potential loss of about 7% was observed, indicating a great potential for industrial application (inset Fig. 4f). Moreover, we also uesed chronoamperometry to test the stability of the catalyst. Fig. S21 shows that the steady current density of Fe_2P-$WO_{2.92}$/NF over a long period of 50 h in 1.0 M KOH. This degradation of catalytic performance may be caused by catalyst exfoliation and morphological agglomeration after long-term operation (Fig. S22).

The turnover frequency (TOF) was calculated to further evaluate the intrinsic OER activities of electrocatalysts using Eq. (2) [45]:

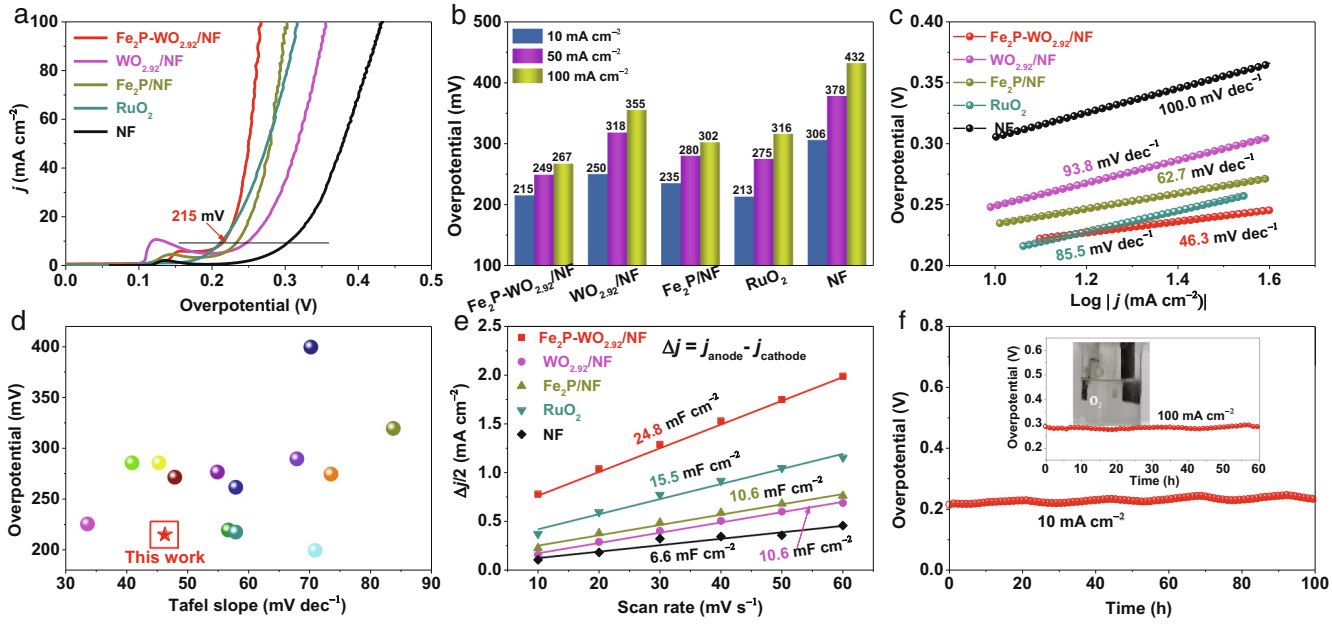

Fig. 4. OER performance of different electrocatalysts in 1.0 M KOH solution. (a) OER polarization curves with a scan rate of 0.2 mV s^{-1}. (b) The overpotential comparison of five catalysts at current densities of 10, 50 and 100 mA cm^{-2}. (c) Tafel plots. (d) Comparison of the overpotential at 10 mA cm^{-2} and Tafel plot of Fe_2P-$WO_{2.92}$/NF with previously reported catalysts. (e) Double-layer capacitance (C_{dl}) plots. (f) Chronopotentiometry curve of Fe_2P-$WO_{2.92}$/NF at a constant current density of 10 mA cm^{-2} for 100 h (Inset: OER stability test of Fe_2P-$WO_{2.92}$/NF at 100 mA cm^{-2} during 60 h and experimental phenomenon during catalyst stability test).

Table 1
The summarized OER catalytic parameters of different catalysts in 1.0 M KOH solution.

Catalysts	η_{10} (mV)	Tafel slope (mV dec^{-1})	C_{dl} (mF cm^{-2})	R_{ct} (Ω)
Fe_2P-$WO_{2.92}$/NF	215	46.3	24.8	0.3
$WO_{2.92}$/NF	250	93.8	10.6	1.7
Fe_2P/NF	235	62.7	10.6	0.6
RuO_2	213	85.5	15.5	0.6
NF	306	100.0	6.6	4.4

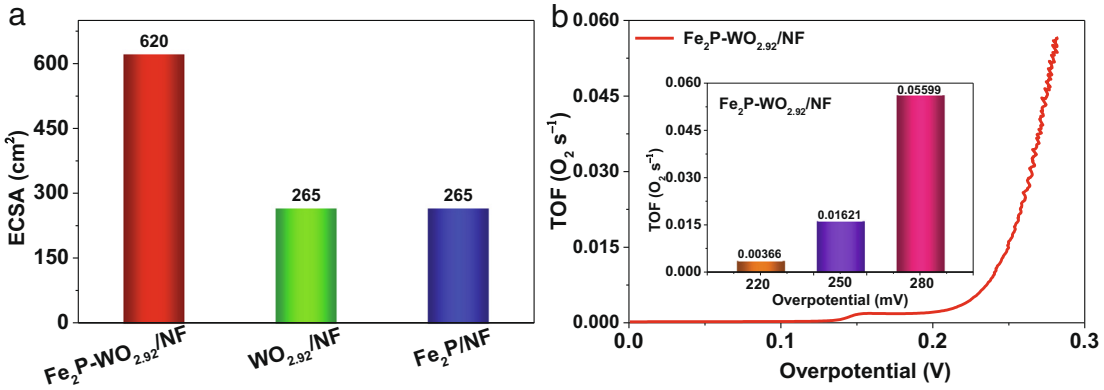

Fig. 5. (a) Comparison the electrochemical active surface area (ECSA) of Fe_2P-$WO_{2.92}$/NF, $WO_{2.92}$/NF and Fe_2P/NF. (b) The turn frequency (TOF) profiles versus overpotential of Fe_2P-$WO_{2.92}$/NF catalyst in 1.0 M KOH solution (Insert: The summarized TOF values at different applied overpotentials of 220, 250 and 280 mV).

$$\mathrm{TOF} = \frac{j \times A}{4Fn} \tag{2}$$

where j is the current density, A is the electrode area with moles of catalyst, F is the Faraday constant (96485C mol^{-1}) and n is the number of active sites of all metals present in the electrode [46,47]. Fig. 5(b) indicates that the TOF value of Fe_2P-$WO_{2.92}$/NF gradually rises when the applied potential increases in alkaline medium. The inset of Fig. 5(b) shows the corresponding TOF value under different overpotentials. When the overpotentials are 220, 250 and 280 mV, the TOF values are 0.00366, 0.01621 and 0.05599 s^{-1} respectively. The small TOF demonstrates the excellent intrinsic catalytic activity of Fe_2P-$WO_{2.92}$/NF [48].

The two-electrode water splitting experiment is a key indicator to decide whether the catalyst can be commercialized [49]. The two-electrode water splitting system was constructed using the Fe_2P-$WO_{2.92}$/NF as anode and commercial Pt/C as cathode as shown in Fig. 6(a). Surprisingly, the Fe_2P-$WO_{2.92}$/$NF^{(+)}$ || $Pt/C^{(-)}$ electrolyzer only needs a cell voltage of 1.49 V to reach the current density of 10 mA cm^{-2} (Fig. 6b), which is a better result than the $RuO_2^{(+)}$ || $Pt/C^{(-)}$ (1.51 V) benchmark. The inset of Fig. 6(b) shows the stability of the catalyst for water splitting, which can be stable for 36 h at 10 mA cm^{-2} without significant attenuation. In addition, we compared the as-prepared electrolyzer with the recently reported two-electrode catalytic configuration, the result elucidates that the cell voltage of the as-prepared catalyst is significantly lower than the most two-electrode systems (Fig. 6c, Table S5). Furthermore, the catalyst was evaluated under industrial relevant condition of 500 mA cm^{-2} current density in 30% KOH solution. As shown in Fig. 6(d), the Fe_2P-$WO_{2.92}$/$NF^{(+)}$ || $Pt/C^{(-)}$ electrolyzer only needs cell voltages of 1.90 V and 1.95 V to drive high current density of 400 and 500 mA cm^{-2}, respectively. Surprisingly, under this condition, the electrolyzer still shows no voltage increase after 42 h at 400 mA cm^{-2} (Inset of Fig. 6d), indicating a great industrial perspective.

Catalytic mechanism analysis

As discussed above, the excellent OER electrocatalytic activity and stability, as well as the outstanding overall water splitting performance of the Fe_2P-$WO_{2.92}$/NF catalyst are considered to be caused by the following reasons. (1) The porous structure can accelerate the transport of electrolyte and gas emission. (2) A higher proportion of oxygen vacancies implies a stronger interaction between Fe_2P and $WO_{2.92}$ components, a faster electron transfer rate and better hydrophilic properties [50]. (3) A larger ECSA value means more active sites, which can promote higher electrocatalytic OER and overall water splitting performance. (4) Electrocatalytic OER involves a four-step process and three intermediates (OH*, O* and OOH*) on the active site in alkaline electrolyte [51]. Previous studies revealed that the introduction of a second component in a hybrid catalyst can optimize the adsorption energy of the active site [52]. In the OER process, part of the Fe_2P component surface will be initially oxidized to Fe oxide/hydroxide, making the contact between Fe_2P and $WO_{2.92}$ components closer [53]. As part of the electrons in the hybrid catalyst are transferred from $WO_{2.92}$ to Fe_2P, the electron-deficient $WO_{2.92}$ component (Lewis acid) is more easily to interact with H_2O molecules (Lewis base) [54], thereby synergistically enhancing the catalytic activity of OER process.

Conclusions

In summary, a high-performance catalyst Fe_2P-$WO_{2.92}$/NF was successful prepared by a simple hydrothermal, soaking and subsequent phosphating treatment. The optimized Fe_2P-$WO_{2.92}$/NF catalyst possesses a porous structure with smooth and interconnected surface, which is able to expose more active sites. In addition, the oxygen vacancies in the catalyst can accelerate electron transfer and optimize adsorption characteristics. The 3D porous NF is used as the substrate for the catalysts growth creating sufficient porosity for releasing the gas bubbles. As a result, the Fe_2P-$WO_{2.92}$/NF catalyst exhibited an excellent OER activity, requiring overpotentials of 215 and 267 mV to achieve current densities of 10 and 100 mA cm^{-2} respectively, and a small Tafel slope of 46.3 mV dec^{-1}

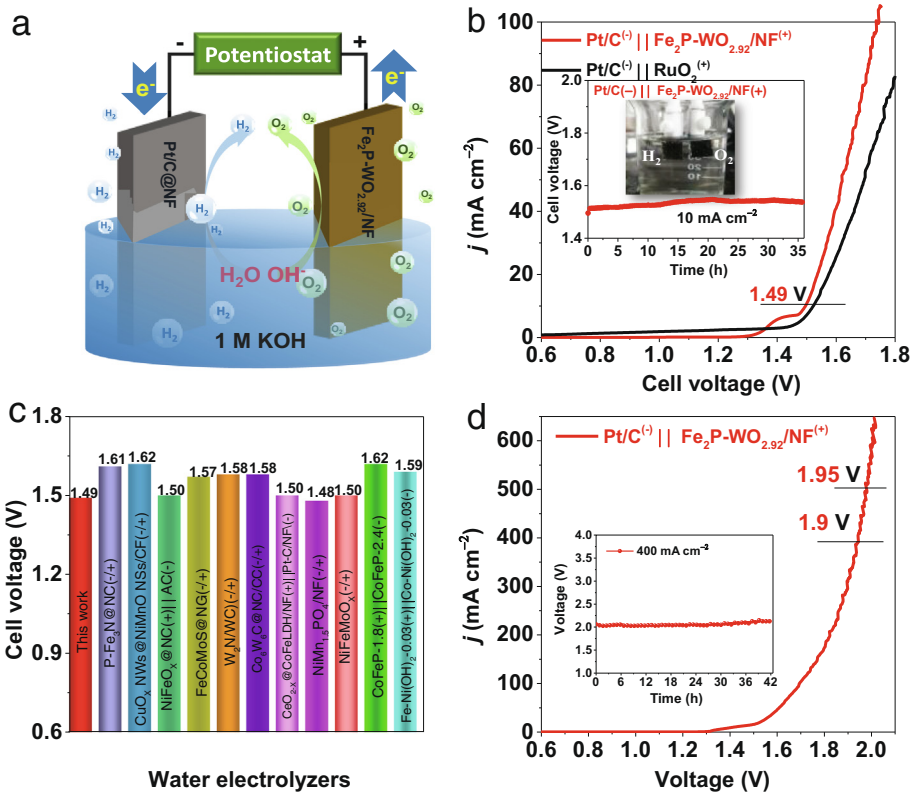

Fig. 6. (a) Schematic description of overall water splitting in two-electrode system. (b) Polarization curves by two-electrode system in 1.0 M KOH electrolyte (Insert: Chronoamperometric curve of Fe_2P-$WO_{2.92}$/$NF^{(+)}$ || $Pt/C^{(-)}$ with the current density of 10 mA cm^{-2} in two-electrode system and experimental phenomenon during catalyst stability test). (c) Comparison of the voltages at 10 mA cm^{-2} with previously reported catalysts in 1.0 M KOH. (d) Polarization curve by two-electrode system of Fe_2P-$WO_{2.92}$/$NF^{(+)}$ || $Pt/C^{(-)}$ in 30% KOH electrolyte (Insert: chronopotentiometry curve of Fe_2P-$WO_{2.92}$/$NF^{(+)}$ || $Pt/C^{(-)}$ with the current density of 400 mA cm^{-2} in two-electrode system).

manifests a fast reaction kinetics. Particularly, the Fe_2P-$WO_{2.92}$/NF catalyst possesses a robust stability at 100 mA cm^{-2} for 60 h without significant attenuation. In addition, the catalyst also exhibits good overall water splitting performance, which is better than most previously reported catalysts. In short, this work provides a rational approach for designing low-cost, high-efficiency and non-noble metal-based electrocatalysts for industrial water splitting.

Declaration of Competing Interest

The authors declare that they have no known competing financial interests or personal relationships that could have appeared to influence the work reported in this paper.

Acknowledgments

This work has been supported by the National Natural Science Foundation of China (no. 21965005), the Natural Science Foundation of Guangxi Province (2018GXNSFAA294077, 2021GXNSFAA076001), the Project of High-Level Talents of Guangxi (F-KA18015), and Guangxi Technology Base and Talent Subject (GUIKE AD18126001, GUIKE AD20297039).

Appendix A. Supplementary data

Supplementary data to this article can be found online at https://doi.org/10.1016/j.jechem.2021.06.037.

References

[1] S.T. Wismann, J.S. Engbæk, S.B. Vendelbo, F.B. Bendixen, W.L. Eriksen, K. Aasberg-Petersen, C. Frandsen, I. Chorkendorff, P.M. Mortensen, Science 364 (2019) 756–759.
[2] J. Chen, B. Ren, H. Cui, C. Wang, Small 16 (2020) 1907556.
[3] Q. Wang, X. Huang, Z.L. Zhao, M. Wang, B. Xiang, J. Li, Z. Feng, H. Xu, M. Gu, J. Am. Chem. Soc. 142 (2020) 7425–7433.
[4] Y.R. Hong, K.M. Kim, J.H. Ryu, S. Mhin, J. Kim, G. Ali, K.Y. Chung, S. Kang, H. Han, Adv. Funct. Mater. 30 (2020) 2004330.
[5] Z. Xiao, Y.C. Huang, C.L. Dong, C. Xie, Z. Liu, S. Du, W. Chen, D. Yan, L. Tao, Z. Shu, G. Zhang, H. Duan, Y. Wang, Y. Zou, R. Chen, S. Wang, J. Am. Chem. Soc. 142 (2020) 12087–12095.
[6] T.H. Shen, L. Spillane, J. Vavra, T.H.M. Pham, J. Peng, Y. Shao-Horn, V. Tileli, J. Am. Chem. Soc. 142 (2020) 15876–15883.
[7] M.A. Ahsan, A.R. Puente Santiago, Y. Hong, N. Zhang, M. Cano, E. Rodriguez-Castellon, L. Echegoyen, S.T. Sreenivasan, J.C. Noveron, J. Am. Chem. Soc. 142 (2020) 14688–14701.
[8] J. Diao, Y. Qiu, S. Liu, W. Wang, K. Chen, H. Li, W. Yuan, Y. Qu, X. Guo, Adv. Mater. 32 (2020) 1905679.
[9] S. Sirisomboonchai, X. Li, N. Kitiphatpiboon, R. Channoo, S. Li, Y. Ma, S. Kongparakul, C. Samart, A. Abudula, G. Guan, J. Mater. Chem. A 8 (2020) 16463–16476.
[10] T. Ouyang, X.T. Wang, X.Q. Mai, A.N. Chen, Z.Y. Tang, Z.Q. Liu, Angew. Chem. Int. Ed. 59 (2020) (1957) 11948–11951.
[11] J. He, X. Zhou, P. Xu, J. Sun, Nano Energy 80 (2021) 105540.
[12] J. Zhang, R. Cui, C. Gao, L. Bian, Y. Pu, X. Zhu, X. Li, W. Huang, Small 15 (2019) 1904688.
[13] H. Yan, Y. Xie, A. Wu, Z. Cai, L. Wang, C. Tian, X. Zhang, H. Fu, Adv. Mater. 31 (2019) 1901174.
[14] H. Sun, Y. Min, W. Yang, Y. Lian, L. Lin, K. Feng, Z. Deng, M. Chen, J. Zhong, L. Xu, Y. Peng, ACS Catal. 9 (2019) 8882–8892.
[15] H. Liu, J. Guan, S. Yang, Y. Yu, R. Shao, Z. Zhang, M. Dou, F. Wang, Q. Xu, Adv. Mater. 32 (2020) 2003649.
[16] L. Wang, Z. Li, K. Wang, Q. Dai, C. Lei, B. Yang, Q. Zhang, L. Lei, M.K.H. Leung, Y. Hou, Nano Energy 74 (2020) 104850.
[17] S. Zhang, G. Gao, H. Zhu, L. Cai, X. Jiang, S. Lu, F. Duan, W. Dong, Y. Chai, M. Du, Sci. Bull. 65 (2020) 640–650.
[18] Z. Chen, R. Zheng, M. Graś, W. Wei, G. Lota, H. Chen, B.-J. Ni, Appl. Catal. B: Environ. 288 (2021) 120037.
[19] M. Jiang, J. Li, J. Li, Y. Zhao, L. Pan, Q. Cao, D. Wang, Y. Du, Nanoscale 11 (2019) 9654–9660.
[20] C.-N. Lv, L. Zhang, X.-H. Huang, Y.-X. Zhu, X. Zhang, J.-S. Hu, S.-Y. Lu, Nano Energy 65 (2019) 103995.
[21] Y. Ling, M. Li, K. Qu, Z. Yang, Chem. Commun. 56 (2020) 15193–15196.
[22] M. Qu, Y. Jiang, M. Yang, S. Liu, Q. Guo, W. Shen, M. Li, R. He, Appl. Catal. B: Environ. 263 (2020) 118324.
[23] B.B. Wang, X.X. Zhong, C.L. He, B. Zhang, U. Cvelbar, K. Ostrikov, J. Alloys Compd. 854 (2021) 157249.
[24] Y. Huang, H. Xu, D. Luo, Y. Zhao, Y. Fang, Q. Guo, Y. Wei, L. Fan, J. Wu, J. Alloys Compd. 806 (2019) 418–427.
[25] A. Han, H. Chen, Z. Sun, J. Xu, P. Du, Chem. Commun. 51 (2015) 11626–11629.
[26] Z. Xia, H. Sun, X. He, Z. Sun, C. Lu, J. Li, Y. Peng, S. Dou, J. Sun, Z. Liu, Nano Energy 60 (2019) 385–393.
[27] P. Yan, M. Huang, B. Wang, Z. Wan, M. Qian, H. Yan, T.T. Isimjan, J. Tian, X. Yang, J. Energy Chem. 47 (2020) 299–306.
[28] S. Zhou, Y. Yang, W. Zhang, X. Rao, P. Yan, T.T. Isimjan, X. Yang, J. Colloid Interface Sci. 591 (2021) 221–228.
[29] N. Han, S. Luo, C. Deng, S. Zhu, Q. Xu, Y. Min, ACS Appl Mater. Interfaces 13 (2021) 8306–8314.
[30] X. Zhong, Y. Sun, X. Chen, G. Zhuang, X. Li, J.-G. Wang, Adv. Funct. Mater. 26 (2016) 5778–5786.
[31] H. Chen, L. Song, S. Ouyang, J. Wang, J. Lv, J. Ye, Adv. Sci. 6 (2019) 1900465.
[32] W. Wang, Z. Yang, F. Jiao, Y. Gong, Appl. Surf. Sci. 529 (2020) 146987.
[33] X. Liu, Y. Yao, H. Zhang, L. Pan, C. Shi, X. Zhang, Z.-F. Huang, J.-J. Zou, ACS Sustainable Chem. Eng. 8 (2020) 17828–17838.
[34] C. Wu, J. Zhang, J. Guo, L. Sun, J. Ming, H. Dong, Y. Zhao, J. Tian, X. Yang, ACS Sustainable Chem. Eng. 6 (2018) 7451–7457.
[35] B. Wang, H. Huang, M. Huang, P. Yan, T.T. Isimjan, X. Yang, Sci. China Chem. 63 (2020) 841–849.
[36] Y. Tang, L. You, K. Zhou, ACS Appl Mater. Interfaces 12 (2020) 25884–25894.
[37] X. Liu, H. Zhai, P. Wang, Q. Zhang, Z. Wang, Y. Liu, Y. Dai, B. Huang, X. Qin, X. Zhang, Catal Sci. Technol. 9 (2019) 652–658.
[38] Y. Zhang, H. Zhang, Y. Feng, L. Liu, Y. Wang, ACS Appl Mater. Interfaces 7 (2015) 26684–26690.
[39] L. Zhuang, L. Ge, Y. Yang, M. Li, Y. Jia, X. Yao, Z. Zhu, Adv. Mater. 29 (2017) 1606793.
[40] J. Guo, B. Wang, D. Yang, Z. Wan, P. Yan, J. Tian, T.T. Isimjan, X. Yang, Appl. Catal. B: Environ. 265 (2020) 118584.
[41] X. Liu, K. Ni, C. Niu, R. Guo, W. Xi, Z. Wang, J. Meng, J. Li, Y. Zhu, P. Wu, Q. Li, J. Luo, X. Wu, L. Mai, ACS Catal. 9 (2019) 2275–2285.
[42] X. Wang, Y. Yang, L. Diao, Y. Tang, F. He, E. Liu, C. He, C. Shi, J. Li, J. Sha, S. Ji, P. Zhang, L. Ma, N. Zhao, ACS Appl Mater. Interfaces 10 (2018) 35145–35153.
[43] M. Wang, W. Zhang, F. Zhang, Z. Zhang, B. Tang, J. Li, X. Wang, ACS Catal. 9 (2019) 1489–1502.
[44] C.C. McCrory, S. Jung, J.C. Peters, T.F. Jaramillo, J. Am. Chem. Soc. 135 (2013) 16977–16987.
[45] Z. Wan, Q. He, J. Chen, T.T. Isimjan, B. Wang, X. Yang, Chinese, J. Catal. 41 (2020) 1745–1753.
[46] B. Liu, Y. Wang, H.Q. Peng, R. Yang, Z. Jiang, X. Zhou, C.S. Lee, H. Zhao, W. Zhang, Adv. Mater. (2018) 1803144.
[47] Y. Hu, H. Yu, L. Qi, J. Dong, P. Yan, T. Taylor Isimjan, X. Yang, ChemSusChem. 14 (2021) 1–10.
[48] Y. Pan, K. Sun, Y. Lin, X. Cao, Y. Cheng, S. Liu, L. Zeng, W.-C. Cheong, D. Zhao, K. Wu, Z. Liu, Y. Liu, D. Wang, Q. Peng, C. Chen, Y. Li, Nano Energy 56 (2019) 411–419.
[49] Y.K. Li, G. Zhang, W.T. Lu, F.F. Cao, Adv. Sci. 7 (2020) 1902034.
[50] M. Li, X. Pan, M. Jiang, Y. Zhang, Y. Tang, G. Fu, Chem. Eng. J. 395 (2020) 125160.
[51] W. Wang, Y. Jiang, Y. Hu, Y. Liu, J. Li, S. Chen, ACS Appl Mater. Interfaces 12 (2020) 11600–11606.
[52] L. Yan, Y. Sun, E. Hu, J. Ning, Y. Zhong, Z. Zhang, Y. Hu, J. Colloid Interface Sci. 541 (2019) 279–286.
[53] L. Huang, Y. Zou, D. Chen, S. Wang, Chin J. Catal. 40 (2019) 1822–1840.
[54] J. Yu, T. Zhang, Y. Sun, X. Li, X. Li, B. Wu, D. Men, Y. Li, ACS Appl Mater. Interfaces 12 (2020) 12783–12792.